Journal of Superconductivity and Novel Magnetism (2020) 33:1187–1198
https://doi.org/10.1007/s10948-019-05343-x

ORIGINAL PAPER

Improved Electromagnetic Interference Shielding Response of Polyaniline Containing Magnetic Nano-ferrites

Sumit Kumar[1,2] · Anil Ohlan[3] · Prashant Kumar[4] · Vivek Verma[1]

Received: 13 June 2019 / Accepted: 19 October 2019 / Published online: 15 November 2019
© Springer Science+Business Media, LLC, part of Springer Nature 2019

Abstract

Improvement of electromagnetic interference (EMI) shielding materials with miniaturization of devices is an important area of research in various applications like communication, electronic warfare, defense, and different civilian applications. Nano-crystalline ferrite, MFe_2O_4 (M = Ni, Zn, and Co), powders have been synthesized by sol-gel citrate nitrate precursor method. The crystalline size of samples was found in the range of 20–45 nm as analyzed by XRD and TEM analysis. Polyaniline/ferrite nano-composites with 50 wt% were synthesized by mechanical blending. The structural and magnetic properties of the nano-particles were characterized by using Rietveld analysis of powder X-ray diffraction and vibrating sample magnetometer (VSM) respectively. Using the Rietveld refinement, the goodness of fit, interatomic distance, Bragg contribution, and *R* factors have been determined. Ferrites and their nano-composites, under applied magnetic field up to 20 KOe, exhibited the hysteresis loops of ferromagnetic nature with maximum saturation magnetization of 51.68 emu/g shown by $CoFe_2O_4$. The electromagnetic shielding parameters (various shielding effectiveness and reflection loss) and microwave absorbing properties were measured in *X* band frequency region (8.2–12.2 GHz). Nano-composites show promising and enhanced EMI shielding behavior with overall highest SE value of 52 dB shown by $CoFe_2O_4$ composite.

Keywords Electromagnetic interference · Nano-composites · Microwave absorption · Sol-gel

1 Introduction

Electromagnetic interference (EMI) shielding can be considered as the reflection and/or adsorption of electromagnetic radiation by a material, which acts as a shield against the penetration of the radiation through it. As electromagnetic radiation, particularly that at high frequencies, tends to interfere with electronics, EMI shielding of both electronics and the radiation source is needed and is increasingly required around the world. EMI shielding is an important tool to the increasing dependence of today's society on the electronic devices and their rapid growth. But with the faster development and miniaturization of electronic devices and communication instruments, the electromagnetic (EM) pollution is widely acknowledged to be a growing and serious problem. This increase in electromagnetic pollution can affect human health [1, 2], as well as the surrounding environment, if no shielding is provided. Also, the interference can result in the malfunction and degradation of electronic devices. Therefore, some shielding mechanism must be provided to prevent the internal components of a device from the surroundings' EMI radiation or to control the electromagnetic energy generated by the device that can escape into the external environment so that the electromagnetic pollution gets minimized [3]. The lifetime and the performance of electronic devices can be increased by proper EMI shielding. Also, various defense and aerospace applications, such as constructing "stealth" aircrafts, necessitate the conception of efficient microwave shielding and absorbing materials.

Whenever an EM radiation interacts with any material or device, three possibilities can be defined either it gets reflected, absorbed, or transmitted. For the purpose of shielding, we need to minimize the transmission of radiation as much as possible.

✉ Vivek Verma
vermavivek.neel@gmail.com; vivekverma@hinducollege.ac.in

[1] Department of Physics, Hindu College, University of Delhi, New Delhi 110007, India

[2] Department of Physics and Astrophysics, University of Delhi, New Delhi 110007, India

[3] Department of Physics, M. D. University, Rohtak 124001, India

[4] AcSIR, National Physical Laboratory Campus, New Delhi 110012, India

So, the main function of EMI shielding is to reflect external EM radiations that interact directly with the EM fields created by the devices so that it can stop their malfunctioning. The reflections of the EM radiations can be achieved with the help of charge carriers of the materials so the material should be conductive for this purpose but this is not the only requirement for a shielding material. Another mechanism of EMI shielding requires absorption of radiations which can occur due to the interaction of materials' electric and/or magnetic dipoles with the incident radiations. This phenomenon can be understood in terms that when the dipoles interact with the radiations, they get oriented and dissipate energy in the form of thermal energy. The electric and/or magnetic dipoles required for absorption of EM radiations may be provided by materials having high value of dielectric constant (e.g., TiO_2, $BaTiO_3$) and magnetic permeability (e.g., Fe metals, γ-Fe_2O_3, Fe_3O_4). In addition to these two mechanisms, there also occur multiple reflections inside the material when EM wave pass through the material. These mechanisms of the interaction of EM radiation followed by a shielding material are represented in Fig. 1.

Conventional EMI shielding materials are usually metals (e.g., Faraday cage), such as copper and aluminum due to their good electrical conductivity. But due to their heavy weight, less mechanical stability, and chemical resistances, they cannot be considered as suitable shielding materials [4]. Many carbon-based materials (e.g., graphene, reduced graphene oxide, carbon nano-tubes) have been reported and regarded as alternatives for EMI shielding applications due to their low density and corrosion resistance. But their performance is lower than that of metals as shielding materials, and also, they have poor dispersibility [5]. Therefore, new investigations are needed to explore other materials which possess the requirements of suitable shielding behaviors. In this regard, the conducting polymer-ferrite composites with both electrical and magnetic properties have received great attention, and the study of this kind of composites has become one of the most promising research areas [6, 7]. Conducting polymers have attracted significantly as EMI shielding materials and among them polyaniline (PANI) has been extensively used and studied due to its good electrical conductivity, high environmental stability, and easy preparation. Besides the good conductivity of PANI to absorb the electromagnetic wave absorption, it has another amorphous structure to increase the electromagnetic wave absorption properties. The metals and PANI-based compositions have received good attention due to their conductivity, adjustable permittivity or permeability, nominal cost, and good stability but they are not easy to process and also have poor mechanical properties [8]. The direct coating of conducting polymers on the surface of textiles is another technique as fabrics have good mechanical properties. But the EMI shielding efficiencies for the fabric-based compositions are very less due to their low conductivity and absence of dielectric or magnetic losses [9, 10]. Therefore, we need good inorganic fillers to the conducting polymers that can reflect or absorb the EM radiations to a much large extent to attain good shielding effectiveness. Over the past decades, the various types of absorbers such as ferroelectric and ferromagnetic materials [11, 12] and also conducting polymers [13, 14] are utilized for this purpose but the modern microwave-absorbing materials cannot meet all of the requirements, such as strong absorption, wide range of absorption frequency, thin thickness, and light weight at the same time. Thus, a combination of magnetic constituents and conducting polymeric materials opens new possibilities to provide electromagnetic shielding. In this regard, the conductive polymer-magnetic ferrite composites are promising candidates for the shielding application due to a hybrid structural and functional combination between the organic and inorganic materials. Nano-

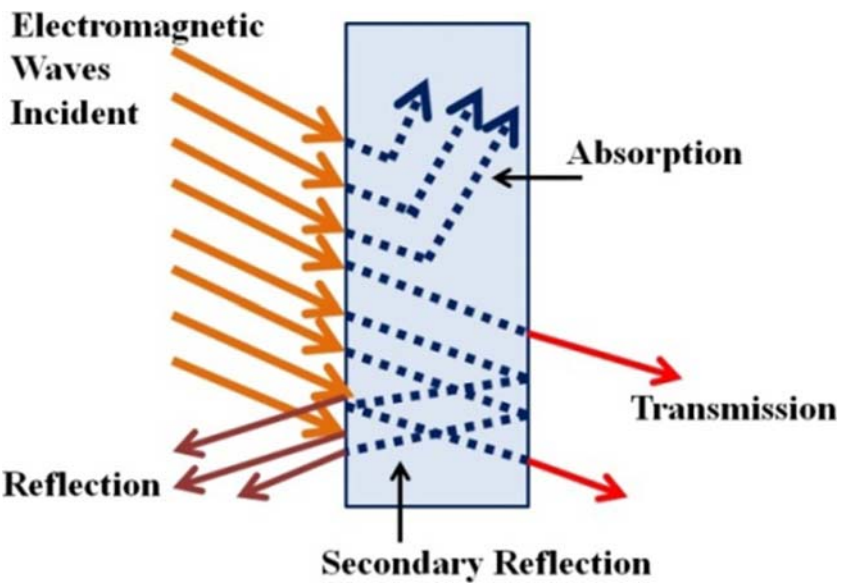

Fig. 1 Schematic descriptions of interaction mechanisms of incident electromagnetic waves with the medium

crystalline ferrites having a general formula MFe_2O_4 (M = divalent metal ion, e.g., Ni, Co, Cu, Mn, Mg, Zn, Cd) are one of the most attractive classes of oxide magnetic materials for these kinds of technological applications. These ferrites have been widely studied due to their high electromagnetic performance, excellent chemical stability and mechanical hardness, coercivity, and saturation magnetization [15–19]. Ferrites and their composites with conducting polymers are good fillers for the development of electromagnetic attenuation materials at microwave, due to their low cost, low density, high stability, saturation magnetization, permeability, resistivity, dielectric constant, adequate magnetic properties, and corrosion resistance (compared to metals and carbon).

This work is motivated in development of magnetic-conducting polymer materials with magnetically and electrically controlled shielding properties to get good shielding effectiveness. Therefore, nano-composites containing polyaniline-ferrite nano-particles ($NiFe_2O_4$, $ZnFe2O_4$, and $CoFe_2O_4$) were synthesized to study the EMI shielding properties.

2 Experimental Details

2.1 Materials Used

Aniline (An), ammonium peroxydisulfate $(NH_4)_2S_2O_8$ (APS), isopropyl alcohol, and ammonium hydroxide solution with all of analytical purity have been purchased from Merck India. Cobalt nitrate ($Co(NO_3)_2.6H_2O$), nickel nitrate ($Ni(NO_3)_2.6H_2O$), zinc nitrate ($Zn(NO_3)_2.6H_2O$), ferric nitrate ($Fe(NO_3)_3.9H_2O$), and citric acid have been obtained from Fischer Scientific (India). Dodecyl benzene sulfonic acid (DBSA) has been purchased from Acros organics (Belgium). All reagents were used without further purification.

2.2 Synthesis of Ferrites Nano-particles

Nano-particles of ferrites were synthesized by using sol-gel method. $Ni(NO_3)_2.6H_2O$ and $Fe(NO_3)_3{\cdot}9H_2O$ were separately dissolved in de-ionized water in stoichiometric amounts. Then, the solutions were mixed with citric acid acting as a reductant taking equal molar ratio of citric acid to the total nitrate precursors and stirred well. The pH of the solution was adjusted to 7 using ammonia solution. The temperature of the solution was then raised from room temperature to about 70 °C and kept constant for few hours. Then the solution became viscous in gel form and very fragile foam was obtained with an exothermic reaction [20]. The dried precursor was then crushed to fine powder. Obtained powder was calcined at 400 °C for 1 h resulting in the phase formation of ferrite. The same steps have been adopted to prepare other ferrites.

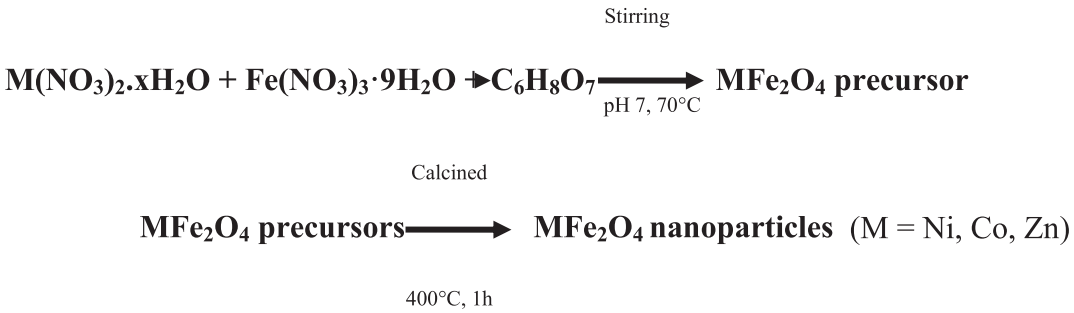

2.3 Synthesis of PANI

PANI in emeraldine state has been synthesized by in situ emulsion polymerization of aniline monomer using DBSA as dopant which also acts as surfactant. In atypical procedure, emulsion solution has been prepared by homogenizing (0.3 M) DBSA to which aniline (0.1 M) has been added and again homogenized for 2 h. The solution of aniline and DBSA has been polymerized by using ammonium peroxydisulfate, $(NH_4)_2S_2O_8$ (0.1 M), as oxidant. The reaction has been allowed to proceed for 6–8 h at temperature below 5 °C. At the end of the reaction, a dark green suspension was formed [21]. The product so obtained has been demulsified using equal amount of propan-2-ol and the product has been filtered, washed repeatedly with distilled water, and dried at 40–50 °C in oven resulting to the formation of conducting polyaniline powder.

2.4 Synthesis of Composites

The composites were prepared by mechanical blending of polyaniline powder with ferrites' nano-particles ($NiFe_2O_4$, $CoFe_2O_4$, and $ZnFe_2O_4$) in 1:1 weight ratio as the best composition. Due to the equal concentration of both materials, there should be better interfacial interaction between them.

The rectangular samples of thickness 2.50 mm were prepared to calculate shielding parameters.

2.5 Characterization

X-ray diffraction (XRD) studies of the samples have been carried out on Bruker D4 X-ray diffractometer using Cu-Kα radiation (λ = 1.5406 Å) in scattering range (2θ) of 25–80° with a scan rate of 0.02°/s. The morphology of ferrite nano-particles has been studied by using transition electron microscopy (TEM) images on Tecnai G2 20 (FEI) S-Twin high-resolution transmission electron microscopy (HRTEM) at an accelerating voltage of 200 kV. The specimens were prepared by sonicating the powdered sample in ethanol for about 30 min followed by uniform disperse solution dropped on the copper grid dried at room temperature. The morphology of PANI/ferrite nano-composites have been examined using a high-resolution scanning electron microscopy (JEOL SEM 610, 30 kV). The magnetic properties of the samples have been recorded by vibrating sample magnetometer (Lakeshore, 7410). Fourier transform infrared (FTIR) spectroscopy has been performed on a Thermo iS 50 FTIR spectrometer in wave transmission mode to identify the structural bonds and attached chemical functional groups present in the ferrite nano-particles. The EMI shielding properties have been measured by a two-port vector network analyzer (Agilent PNAN5244A) using the waveguide method in *X* band frequency region of 8.2–12.4 GHz by computing *S* parameters.

3 Results and Discussions

3.1 Structural Analysis

The crystalline phase of all the ferrite samples has been identified at room temperature using XRD. Figure 2 shows the XRD patterns of all the pure ferrite samples ($NiFe_2O_4$, $ZnFe_2O_4$, and $CoFe_2O_4$) and their composites with PANI in 2θ range of 20°–80° (JCPDS Card No. 80-0389). XRD patterns of all the ferrite particles present the spinel structure and are well indexed to (111), (220), (311), (222), (400), (422), (511), and (440) crystal planes of cubic spinel phase. The XRD patterns of the nickel and zinc ferrite particles contain the extra reflections of iron oxide with the crystal planes (1 0 4) and (0 2 4) at 2θ values around 33° and 50° respectively. The formation of the secondary phase may be due to the low-temperature synthesis. The XRD patterns of the ferrite samples have broad peaks which indicate the small crystalline size in the samples, due to low-temperature synthesis. The typical XRD pattern of PANI (Fig. 3c) shows broad diffraction peak centered at 25.2°. The curve exhibits a diffuse broad peak suggesting that the pure PANI is amorphous. All the X-ray diffraction patterns of the ferrite nano-particles were analyzed

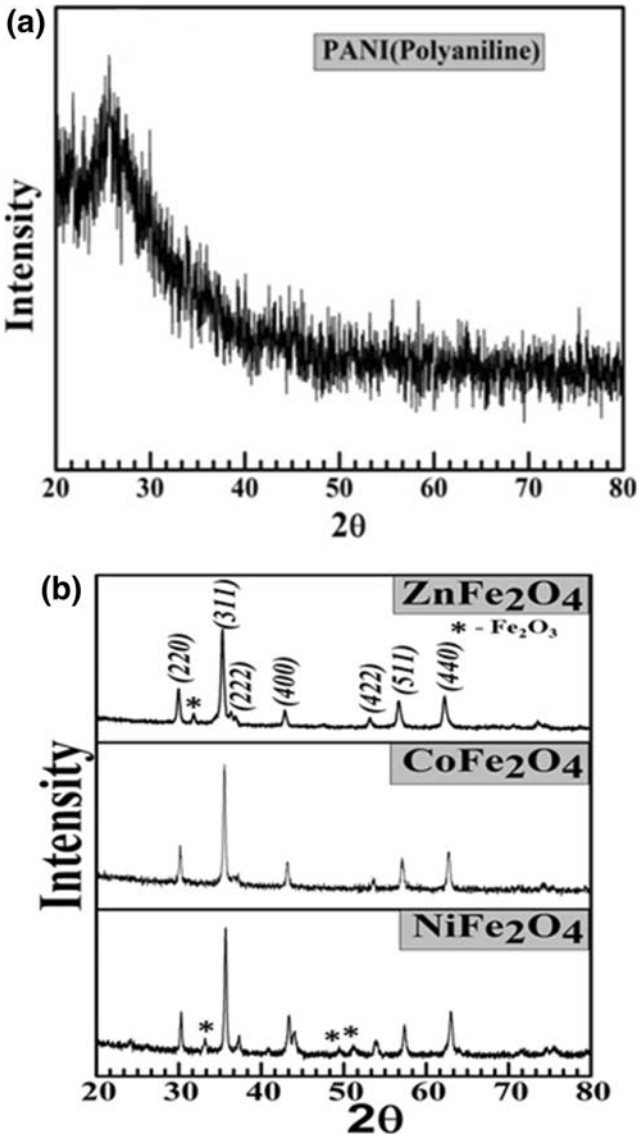

Fig. 2 X-ray diffraction (XRD) pattern of **a** PANI and **b** $NiFe_2O_4$, $CoFe_2O_4$, and $ZnFe_2O_4$ nano-particles in the 2θ range 20°–80°

with the help of FullProf program by employing Rietveld refinement technique.

The analysis of peak shape and width (full width at half maximum) of the Bragg peaks of the X-ray diffraction pattern provides information on the crystallite size and strain. Crystallite size is a measure of the size of a coherently diffracting domain due to the presence of polycrystalline aggregates. It refers to the size of crystal with all its defects and disorders; if every particle is a single crystal then particle size is also equal to crystallite size. XRD can be utilized to evaluate peak broadening with crystallite size and lattice strain. Peak broadening comes from several sources, i.e., instrumental effect, finite crystallite size, and strain effect within the crystal lattice [22]. Taking care of all the sources, crystallite size has been calculated using Scherrer's formula which includes the peak broadening. In Scherrer's formula, the average crystallite

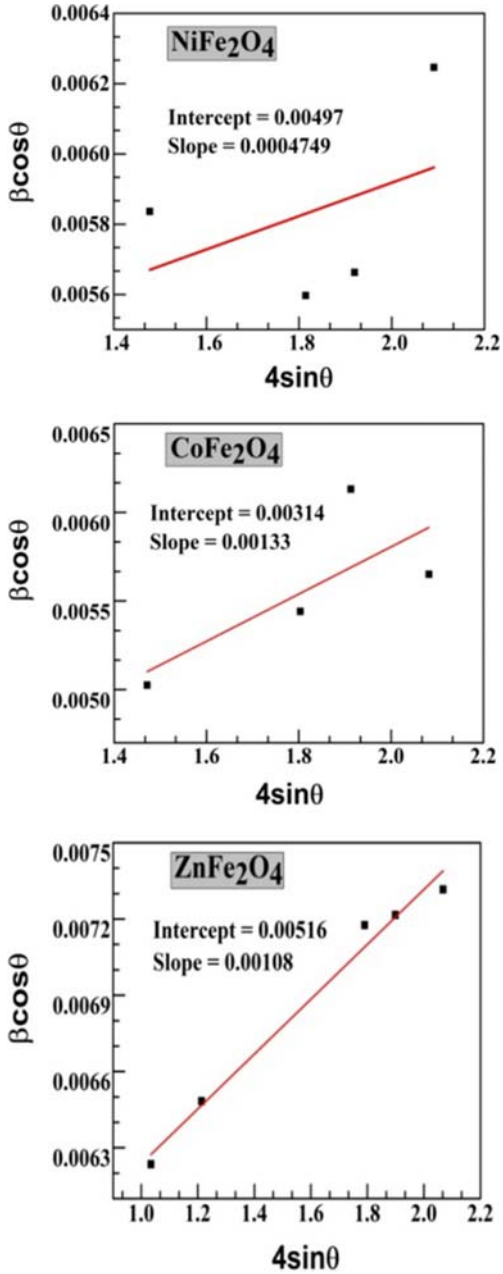

Fig. 3 **a**–**c** Linear regression curves for crystallite size estimation using the Williamson-Hall method (strain broadening) between

size has been calculated using Gaussian fit for the peaks in XRD pattern. The Scherrer formula is given by the following relation:

$$D = \frac{k\lambda}{\beta\cos\theta}$$

where constant k depends upon the shape of the crystallite size (which is equivalent to 0.89, assuming the circular grain), β is the full width at half maximum of the intensity (a.u.) versus 2θ profile, λ is the wavelength of the Cu-Kα radiation (equal to 1.5406 Å), θ is the Bragg diffraction angle, and D is the crystallite size. This equation represents broadening that is due to the finite size of the crystal and it is evident from the equation that size broadening is independent of the order of reflection. Therefore, this method is not suitable for the study of crystals where the strain broadening plays an important role in peak broadening.

According to the Williamson-Hall method [22], the broadening of peaks can be expressed by taking into account the microstrain broadening factor given by following relation:

$$\beta\cos\theta = \frac{k\lambda}{D} + 4\varepsilon\sin\theta$$

where $4\varepsilon\sin\theta$ is the strain effect on the crystallites which arises due to imperfections within the crystalline lattice, including vacancies, dislocations, stacking faults, and others [23]. A plot is to be drawn between $4\sin\theta$ and $\beta\cos\theta$ for the determination of crystallite size. From the linear fit to the data, the crystalline size can be estimated from the y-intercept and the strain ε, from the slope of the fit. Figure 3 shows the linearly fitted curves of the Williamson-Hall method for the pure ferrite nano-particles along with the slope and intercept values of best fitted lines to the data.

From Table 1, it can be concluded that there is a difference in the crystallite size calculated by Scherrer's method and Williamson-Hall method. Particle size was also computed with the help of TEM analysis and it has been found that particle size is in agreement with the size measured using Williamson-Hall method. So, the Williamson-Hall method gives crystallite size distribution more accurately as it includes the strain parameters, separates the instrumental and sample broadening effects, and has length average size rather than the volume average size. Also, all the samples were prepared under identical conditions, but their crystallite sizes were not the same. This may be due to different reactivity of different elements and also due to the fact that the crystallite size is related to the relative interdependence between the nucleation and growth steps and it is strongly affected by the synthesis route which gives different rates of ferrite formation [24–26].

Lattice constant "a" can be calculated from the miller indices (h, k, l) using the relation, $a = d(h^2 + k^2 + l^2)^{1/2}$, where d is the interplanar spacing calculated by using the Bragg law. From the

Table 1 Crystallite sizes of pure ferrite nano-particles estimated using the Scherrer and Williamson-Hall method

Compound	Crystallite size d (nm)	
	Scherrer's method	Williamson-Hall method
NFO	24.4	27.6
CFO	29.0	43.7
ZFO	19.7	25.1

Table 2 Lattice parameters of the ferrite nano-particles

Compound	Lattice constant (**A**)	Density (g/cm^3)	Hopping length L_a (A)	Hopping length L_b (A)
NFO	8.3402	4.0251	3.6114	2.9487
CFO	8.3408	3.9559	3.6016	2.9089
ZFO	8.4258	4.0026	3.6484	2.9784

lattice constant, we can estimate hopping phenomena which gives an idea of the conduction states. In polycrystalline solids, localized states are considered at the band edges (due to the lack of long-range orders) where conduction is possible only by hopping process using thermal energy [27]. The conductivity of solids is inversely proportional to hopping length and directly proportional to the hopping rate of electrons [28]. The shortest distance between magnetic ions occupied at tetrahedral (*A*) and octahedral (*B*) lattice sites considering lattice constant, known as hopping length, can be calculated by using the following relation [29]: $L_A = a\sqrt{3}\,4$ and $L_B = a\sqrt{2}\,4$.

From Table 2, it can be seen that cobalt ferrite has the smallest values of hopping lengths among the synthesized ferrite nano-particles which is due to its high conductivity, whereas zinc ferrite has very low conductivity and large values of hopping lengths.

Also, the density of the samples has been calculated with the XRD patterns using the following relation:

$$\text{Density}, \rho = \frac{ZM}{NV}$$

where Z is the coordination number, M is molecular mass of the samples, N is the Avogadro number, and V is the cell volume for the samples. The values of crystallite size, hopping lengths, and X-ray density for the samples are shown in Table 2.

In an ideal inverse spinel structure, all M^{2+} ions are in B sites and Fe^{3+} ions are equally distributed between A and B sites [30, 31]. Based on the abovementioned, the Rietveld refinement of X-ray diffraction patterns for all the ferrite samples ($NiFe_2O_4$, $CoFe_2O_4$, and $ZnFe_2O_4$) is carried out and shown in Fig. 4. The Rietveld structure refinement was carried out using FULLPROF-suite software from X-ray powder diffraction data. The Rietveld method is a well-established technique for extracting structural details from powder diffraction data. The method employs a least square procedure to compare Bragg intensities and those calculated from a possible structural model. In the first step of refinement, the global parameters, such as background and scale factors, were refined. In the next step, the structural parameters such as lattice parameters, profile shape and width parameters, preferred orientation, asymmetry, isothermal parameters, atomic coordinates, and site occupancies were refined in sequence. The fitting quality of the experimental data is assessed by computing the parameters such as the "goodness of fit" χ^2 and the R factors (R_P = profile factor, R_B = Bragg factor, and R_F = crystallographic factor) [24].

The solid line in Fig. 4 is the best fit to the scattered data, the vertical lines show the positions for the allowed reflections

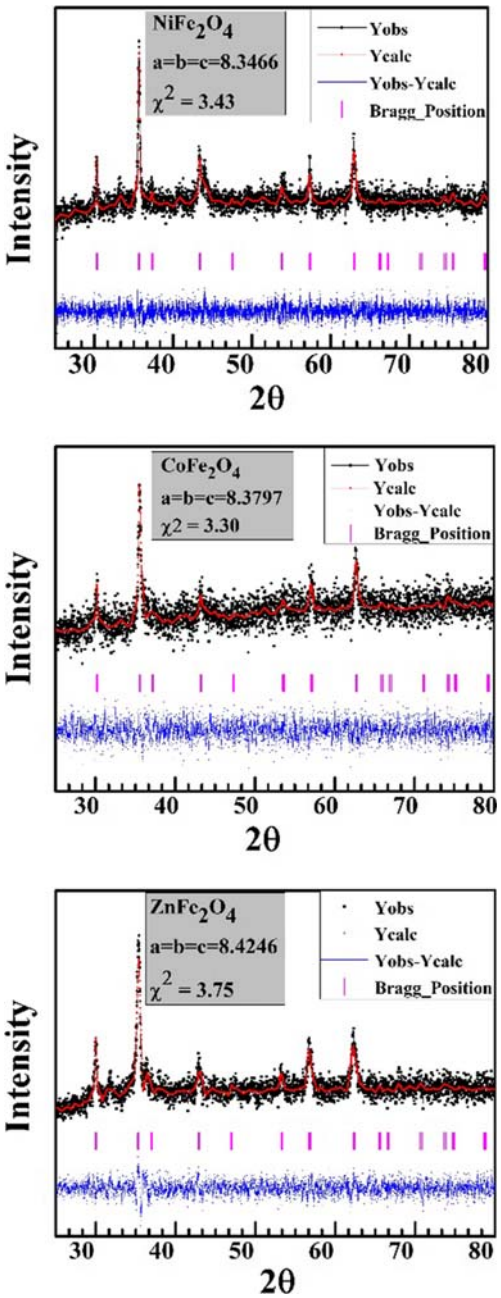

Fig. 4 Rietveld refinement curves for the ferrites ($NiFe_2O_4$, $ZnFe_2O_4$, and $CoFe_2O_4$) with the values of lattice constants and "goodness of fit" χ^2

Table 3 Rietveld refinement parameters for the ferrite nano-particles

Compounds	χ^2	Lattice constant ($a = b = c$)	Direct cell volume	Rwp (discrepancy factor)	Rexp (expected values)	Bragg contribution	Rf (crystallographic factor)
NFO	3.84	8.3403	580.17	4.10	2.65	12.02	13.20
CFO	3.43	8.3889	589.52	3.40	2.32	10.62	18.49
ZFO	3.95	8.4346	600.07	4.59	2.95	12.07	27.49

or Bragg positions for the space group, and the lower curve represents the difference between the observed and the calculated profiles. The refined XRD patterns show that the samples are in single-phase form. The structural model and initial structural parameters were taken as follows: space group Fd-3m, metal and iron atoms were in 8a and 16d special position, and oxygen atom in 32e spatial positions [32]. The refinement is done using the pseudo-Voigt profile function. The value of all the refinement parameters such as the "goodness of fit" $\chi 2$, the R factors (R_P = profile factor, R_B = Bragg factor, and R_F = crystallographic factor), lattice constant parameters, and the direct cell volume for all the ferrite samples are shown in Table 3.

The TEM micrographs of MFe_2O_4 (M = Ni, Co, and Zn) samples are shown in Fig. 5 with average particle size of 28 nm, 44 nm, and 21 nm respectively. The difference of reactivity of the elements is considered to be the dominant reason for difference in the particle size. TEM images indicate that ferrite nano-particles are agglomerated in nature with irregular shapes. The magnetic interaction between nano-particles of the ferrite may be responsible for the agglomeration in powder samples. Figure 5 shows the high-resolution TEM (HRTEM) images of ferrite nano-particles exhibiting interplanar spacing values with their corresponding lattice planes. For $NiFe_2O_4$ sample, the observed d-spacing values are 0.2512 nm and 0.2875 nm associated with the (311) and (220) planes respectively. $CoFe_2O_4$ HRTEM micrograph shows the lattice plane (220) with interplanar d-spacing value 0.2882 nm. $ZnFe_2O_4$ sample has the d-spacing values 0.4991 nm, 0.2497 nm, and 0.2191 nm indexed to the lattice planes (111), (311), and (400) respectively. Figure 5 shows the selected area electron diffraction (SAED) patterns for the ferrite samples having spotty rings indexed to the corresponding lattice planes. Diffraction rings clearly visible in SAED patterns infer the polycrystalline nature of the ferrite samples. In the SAED patterns, the observed rings have been labeled to miller indices (220), (311), (400), (422), and (511) corresponding to the lattice planes of cubic spinel structure while $ZnFe_2O_4$ also shows the (111) plane.

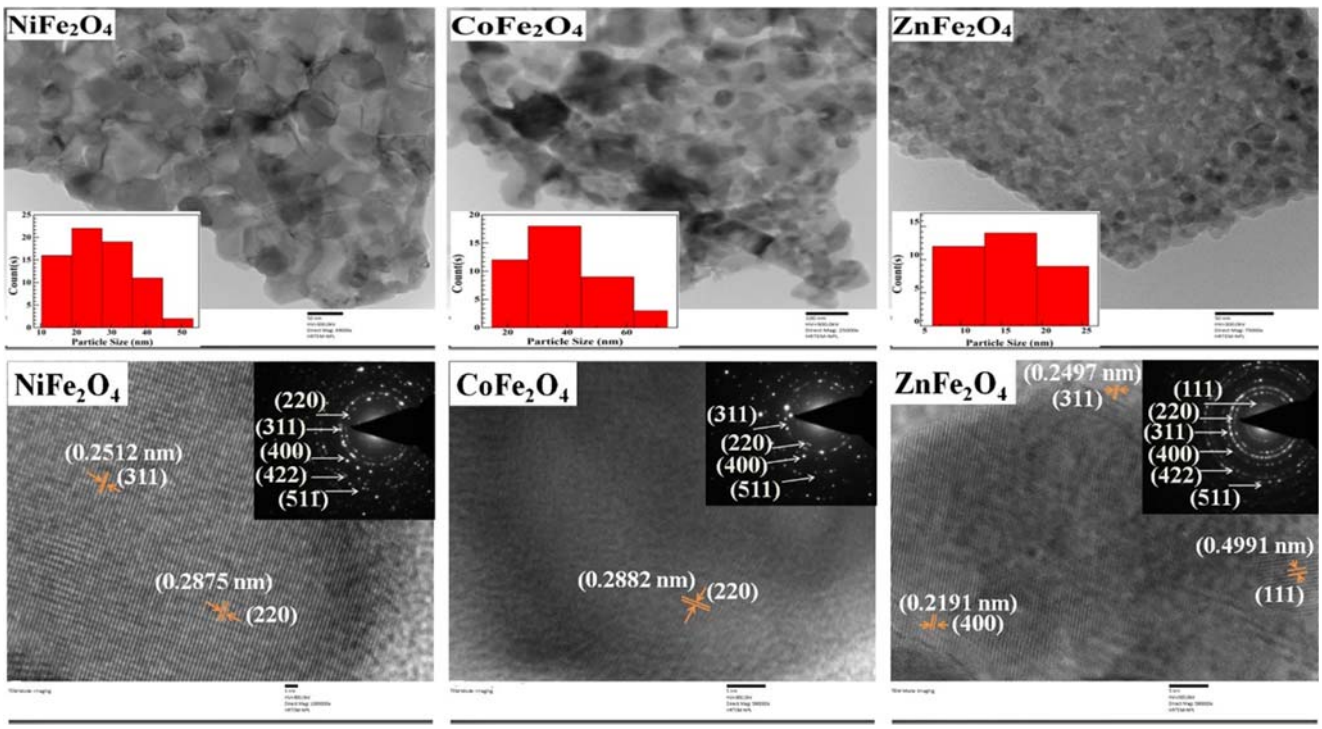

Fig. 5 TEM micrographs (TEM, HRTEM, and SAED) of MFe_2O_4 (M = Ni, Co, and Zn) spinel ferrites

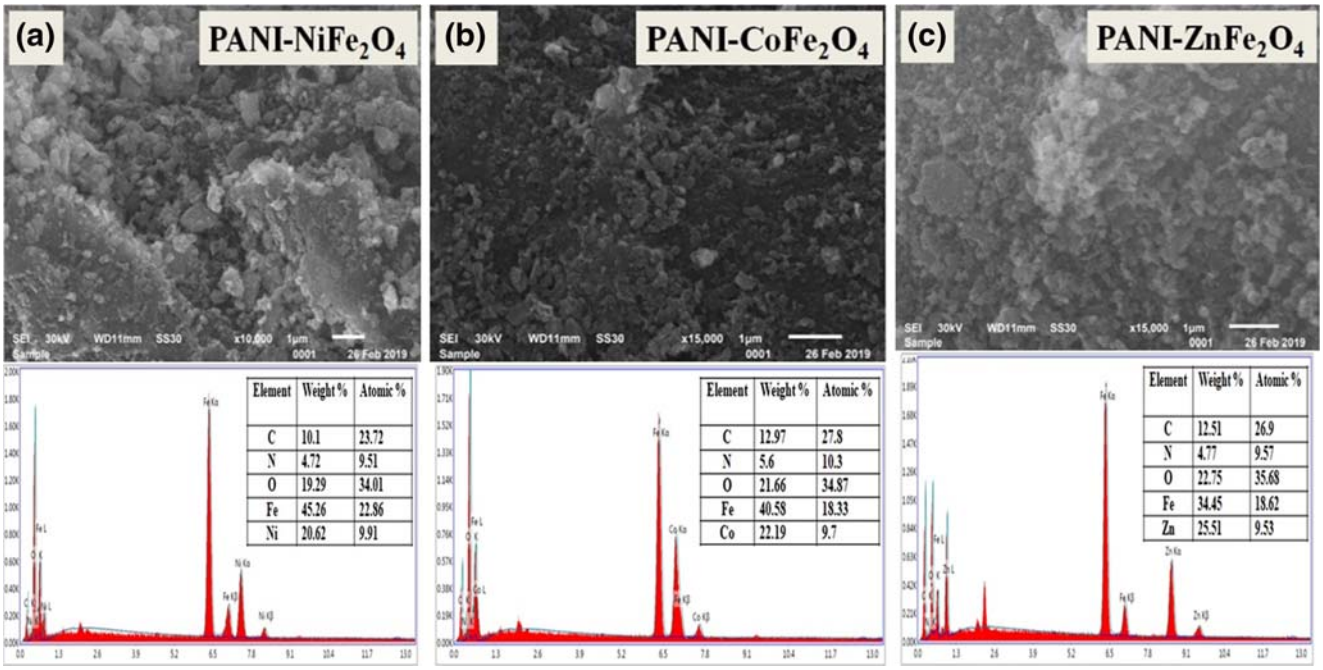

Fig. 6 **a**–**c** SEM micrographs and energy-dispersive X-ray (EDX) patterns for the PANI-ferrite composites ($NiFe_2O_4$-PANI, $CoFe_2O_4$-PANI, and $ZnFe_2O_4$-PANI)

3.2 Surface Morphology

The morphology of PANI/MFe_2O_4 (M = Ni, Co, and Zn) nano-composites were determined by SEM. Figure 6 depicts SEM micrographs of composites of ferrite nano-particles with PANI and the corresponding elemental mapping images for each composite. The SEM images show that the polyaniline is deposited on the surface of ferrite particles and the ferrite particles are finely dispersed in the polymer matrix. The irregular shapes and the porous nature of the compacted powders are evidenced by the images taken at high magnification. These figures show that the surface of these nano-composites is rough and exhibits irregular morphology with the agglomeration of the ferrite nano-particles. The elemental mapping results indicate that C, N, Fe, and M (M = Ni, Co, and Zn) are homogeneously distributed throughout the nano-composites and the strong peaks for the elements are noted in the EDX spectrum. The results obtained are quite similar to other systems reported in the previous studies by the various researchers [33–35].

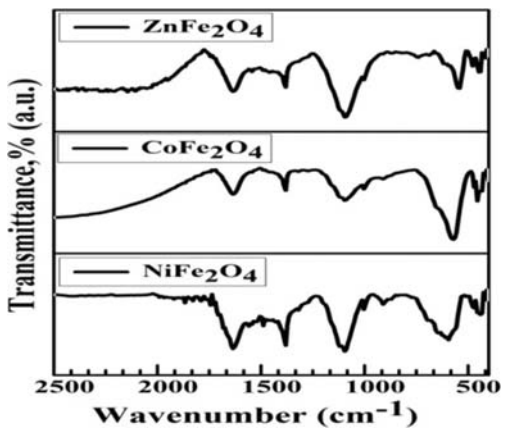

Fig. 7 Comparison of FTIR spectra of $NiFe_2O_4$, $CoFe_2O_4$, and $ZnFe_2O_4$ nano-particles

3.3 FTIR Spectra

Figure 7 shows the FTIR spectroscopy of $NiFe_2O_4$, $CoFe_2O_4$, and $ZnFe_2O_4$ nano-particles. The IR absorption bands of solids in the range 100–1000 cm^{-1} are usually assigned to vibrations of ions in the crystal lattice. In ferrites, the metal ions are situated in two different sub-lattices, designated as tetrahedral and octahedral according to the geometrical configuration of the oxygen nearest neighbors [17]. FTIR spectrum in Fig. 7 shows two bands in the region 400–600 cm^{-1} which are attributed to ferrites. The vibrational spectra of spinel ferrites (MFe_2O_4) are linked to high-frequency band (600–550 cm^{-1}) for the intrinsic vibration of the tetrahedral sites and the low-frequency band (450–400 cm^{-1}) for the octahedral sites [36]. The peaks at 592, 572, and 546 cm^{-1} correspond to tetrahedral sites of $NiFe_2O_4$, $CoFe_2O_4$, and $ZnFe_2O_4$ respectively while peaks at 446, 452, and 438 cm^{-1} correspond to octahedral sites. Also, the bands with peaks at about 1090 and 1600 cm^{-1} can be seen in the figure which can be assigned to adsorption of water on the surface of the ferrites and the

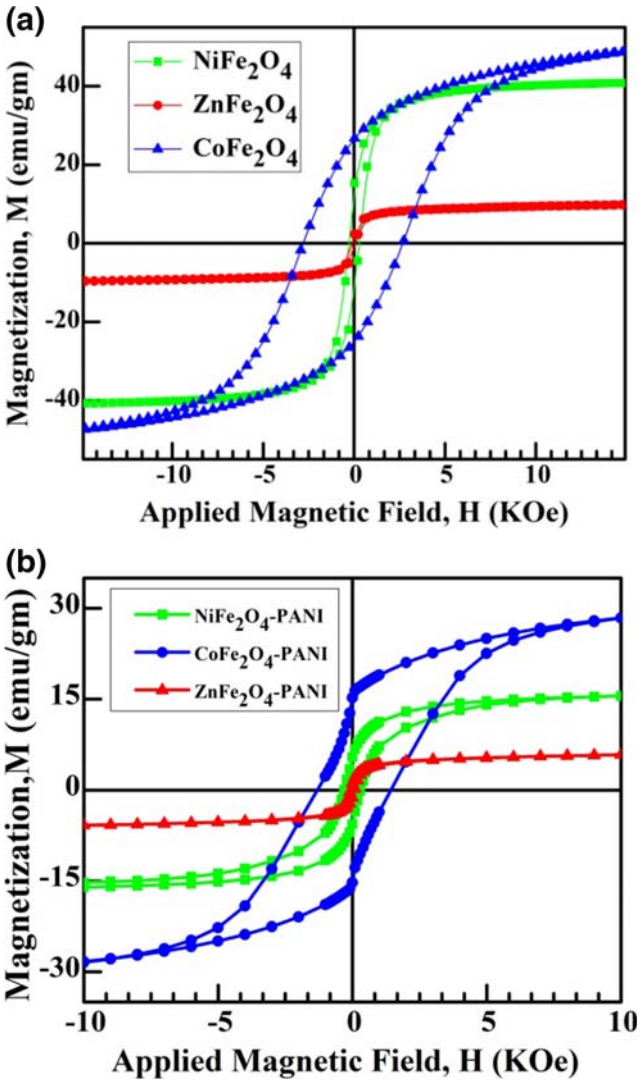

Fig. 8 *M-H* loops of **a** ferrite nano-particles and **b** PANI-ferrite composites, at room temperature

stretching of O–H bonds of the adsorbed H_2O due to hydrogen bonding interactions.

3.4 Magnetic Measurements

The magnetic properties of the ferrites' nano-particles ($NiFe_2O_4$, $CoFe_2O_4$, and $ZnFe_2O_4$) and their composites with the PANI were investigated by VSM. Figure 8 shows the magnetization (M) versus the applied magnetic field (H) loops for ferrites' nano-particles and composites at room temperature. The magnetic parameters such as saturation magnetization (M_s), remnant magnetization (M_r), and coercivity (H_c) that were determined by the hysteresis loop measurements are tabulated in Table 4. It can be observed that the M_s exhibited by $CoFe_2O_4$ is 51.68 emu/g. Cobalt ferrite is a well-known hard magnetic material with high coercivity and magnetization. Hysteresis loop of $NiFe_2O_4$ shows essentially small coercivity and high magnetization with value of 40.68 emu/g. Zinc ferrite being the soft magnetic material due to presence of non-magnetic zinc exhibits smaller value of saturation magnetization of 10.06 emu/g. This smaller value of magnetization in nano-particle comparison to polycrystalline samples can also be attributed to their small crystallite size which leads to the relatively dead or inert surface layers that have low magnetization. This surface effect becomes less significant with increasing size of the nano-particles. So, the observed magnetic properties for the ferrite nano-particles can be concluded due to a combination of many mechanisms, such as magnetocrystalline anisotropy, surface anisotropy, and inter-particle interactions [37].

Figure 8b shows the magnetic behavior for the PANI-ferrite composites at room temperature. Saturation magnetization value reduces for the composites than the pure ferrites due to the existence of non-magnetic medium of PANI polymer in composite as depicted in Table 4. Saturation magnetization in ferrite-PANI composite can be explain by the equation, $MS = \phi \times ms$, where ϕ is the volume fraction of the magnetic particles and m_s is the saturation moment of a single particle in the total sample volume. This means that the total magnetic behavior of the nano-composite could be tuned and tailored by the addition of nonmagnetic medium to a magnetic phase. Nonmagnetic PANI isolates the magnetic particles, which results in the transformation of the collinear ferromagnetic order of ferrites into a noncollinear arrangement. The ferrite nano-particles have an irregular structure, geometric, and crystallographic nature, such as pores, cracks, surface roughness, and impurities. Depositing PANI on the ferrite surface and crystallite boundary reduces the ferrite surface defects, such as pores and cracks, leading to a decrease in magnetic surface anisotropy of ferrite particles, due to which PANI/ferrite nano-composites present a lower value of coercivity than that of pure nano-ferrites [38, 39].

3.5 Shielding Properties

EMI shielding effectiveness is an ability of the materials to attenuate the electromagnetic wave strength, which is defined as the logarithm of incoming power (P_i) to transmitted power (P_t) of an electromagnetic wave in decibels (dB):

$$\text{Shielding Effectiveness (dB)} = 10 \log \left(\frac{Pi}{Pt}\right)$$

There are three typical processes when an electromagnetic wave interacts with a shielding material. Part of the electromagnetic wave is reflected on the surface of the material when interacting with charge carriers (such as electrons); part of the electromagnetic wave is absorbed and dissipated in the form of a leaking current or heat due to the interaction with the electric or magnetic dipoles of the material; part of the electromagnetic wave is multi-reflected inside the shielding material because of

Table 4 Magnetic parameters such as saturation magnetization (M_S), coercivity (H_C), and remanent magnetization (M_r) of ferrites and PANI/ferrite nanocomposites

Compound	Saturation magnetization (emu/g)	Remnant magnetization (emu/g)	Coercivity (Oe)
NFO	40.68	13.94	283.80
CFO	51.68	26.45	2790.00
ZFO	10.06	1.86	92.90
NFO-PANI	16.52	6.45	301.80
CFO-PANI	28.42	15.23	1438.60
ZFO-PANI	5.84	1.15	83.20

the interfaces or defect sites within the material. Since multi-reflected waves get absorbed or dissipated as heat in the same way as the absorbed waves, hence the total EMI shielding effectiveness is dominated by two factors: reflection (R) and absorption (A). Based on the description above, the total EMI SE (SE_T) can be written as, $SE_T = SE_R + SE_A$. These various shielding effectiveness (SE_R, SE_A) can be determined using the reflection, transmission, and absorption parameters of the interacting EM wave. The reflection coefficient (R), transmission coefficient (T), and absorption coefficient (A) were calculated by the S parameters (S_{11} or S_{22} and S_{21} or S_{12}) in a two-port network, according to the following equations [40]:

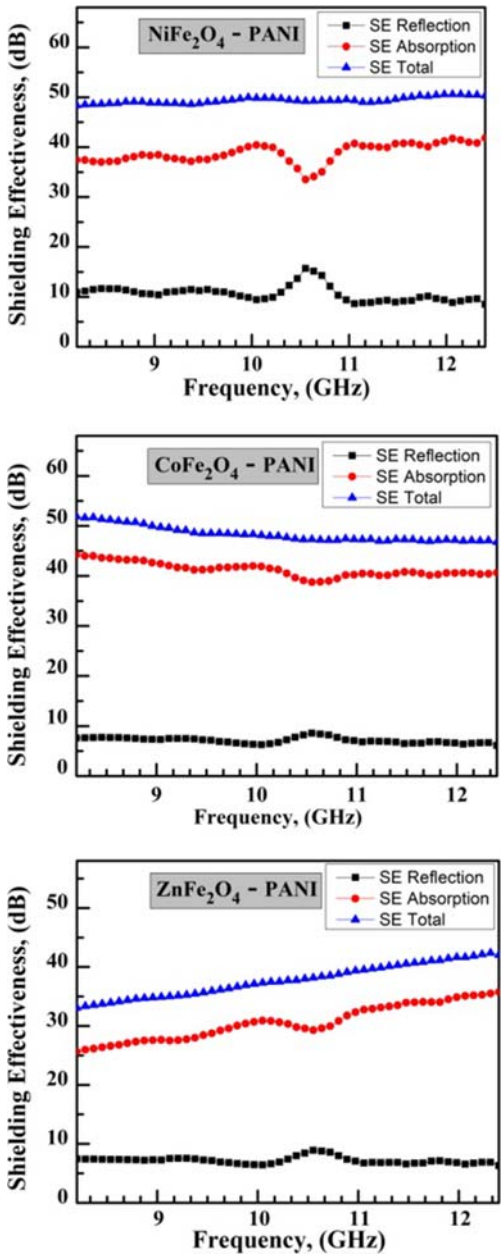

Fig. 9 Dependence of shielding effectiveness (SE_A and SE_R) of composites as a function of frequency

$$T = |E_T/E_I|^2 = |S_{21}|^2 = |S_{12}|^2,$$

$$R = |E_R/E_I|^2 = |S_{11}|^2 = |S_{22}|^2 \quad \text{and}$$

$$A = 1-R-T$$

Effective absorbance (A_{eff}), the absorption efficiency for the electromagnetic wave that propagates in shielding material, can be described as

$$A_{eff} = \frac{(1-R-T)}{(1-R)}$$

So, the shielding effectiveness due to various aspects (SE_A, SE_R, and SE_T) can be finally expressed as:

$$SE_R = -10\log(1-R) = -10\log(1-|S_{11}|^2)$$

$$SE_A = -10\log(1-A_{eff}) = -10\log\left(\frac{T}{(1-R)}\right) = 10\log\left(\frac{(1-|S_{11}|^2)}{|S_{21}|^2}\right)$$

$$SE_T = SE_R + SE_A = -10\log(|S_{21}|^2)$$

Also, according to shielding theory, shielding efficiency (SE) is dependent on a complex function of permittivity and permeability as follows [41]:

Table 5 A comparison of shielding effectiveness characteristics of the current materials with materials in the literature

Shielding material	Shielding performance (dB)	Thickness (mm)	Frequency region (GHz)	Reference
$CoFe_2O_4$/PANI	SE = 52.0	2.5	8.2–12.4	Present work
$NiFe_2O_4$/PANI	SE = 49.0	2.5	8.2–12.4	Present work
$ZnFe_2O_4$/PANI	SE = 42.0	2.5	8.2–12.4	Present work
$CoFe_2O_4$/PANI	SE = 23.0	3.0	8.2–12.4	[43]
$CoFe_2O_4$/rGO	RL = 25.4	2.3	2–18	[44]
$CoFe_2O_4$/PANI	SE = 23.5		12.4–18	[45]
$NiFe_2O_4$/PANI	RL = 20.3	2.0	2–8	[46]
$NiFe_2O_4$/rGO	RL = 27.7	3.0	2–18	[47]
$NiFe_2O_4$/Graphene	RL = 40.9	2.0	2–18	[48]
$MnFe_2O_4$/PANI	RL = 15.3	1.4	8–12	[49]
$Mn_{0.5}Zn_{0.5}Fe_2O_4$/PANI	SE = 20.0			[50]
Fe_3O_4/PANI	SE = 12.3	5.0	7.5–13	[51]
$Ni_{0.5}Zn_{0.5}Fe_2O_4$/PANI	RL = 39.6	2.5	7.5–13	[52]

$$SEA = 20d(\mu r\omega\sigma)1/2\ \log10(e)$$

$$SER = 10\ \log10\left(\frac{\sigma}{16\mu r\omega\varepsilon r}\right)$$

$$SET = 20d\left((\mu r\omega\sigma)1/2\ \log10(e) + 10\ \log10\left(\frac{\sigma}{16\mu r\omega\varepsilon r}\right)\right)$$

where d is sample thickness (cm), e is Napier number (2.718), σ is electrical conductivity ($\sigma = 2\pi f\varepsilon''$) (S/cm), μ_r is relative magnetic permeability, $w = 2\pi f$ is angular frequency, and ε_o is dielectric constant of vacuum.

Generally, the EMI SE of conductive materials is a function of the frequency, thickness, and conductivity [42]. Present work deals with shielding study in X band frequency region of conducting polymer as host matrix having ferrite absorber in the ratio of 1:1 with materials' thickness of 2.50 mm. Figure 9 shows the variation of SE of the ferrite-PANI composites in the X band frequency range (8–12.4 GHz). It is well known that pure ferrites and pure PANI have not good microwave absorption properties. From the Fig. 9, it can be concluded that the composites have an enhanced shielding effectiveness and microwave absorption characteristics. Among all the composites, CFO-PANI have the highest shielding effectiveness with value of 52 dB which may be due to highest magnetization of cobalt ferrite as magnetic dipoles are also responsible for absorption. ZFO-PANI composites have a total shielding effectiveness lying in the range of 32–42 dB which is quiet less than of nickel and cobalt ferrite composites as the absorber, zinc ferrite is a soft magnetic material having low magnetization, whereas NFO-PANI composite has the shielding effectiveness of 49 dB having magnetic properties intermediate to the CFO and ZFO. From Fig. 9, we can observe the cooperative effect of combining ferrites (with a magnetic loss mechanism) and PANI (with a dielectric loss mechanism) on the microwave properties of the absorber. This combination leads to an efficient and lightweight microwave absorber with a wide bandwidth.

In the present work, we obtained the improved shielding properties for PANI-ferrite composites with comparison to the previously reported works which are depicted in Table 5. The table exhibits the shielding effectiveness of composites of ferrite materials with the polyaniline in various frequency regions reported in the literature. It can be observed from the table that improved shielding properties have been achieved for polyaniline containing magnetic nano-ferrites as compared to the previously reported studies. The composites showed an excellent shielding effectiveness with almost steady response in the entire X band frequency range which makes them suitable candidates as EMI shielding materials.

4 Conclusions

We have synthesized the nano-sized ferrite particles by the sol-gel process with low annealing temperature and their composites with PANI by mechanical blending. The magnetic properties of nickel and cobalt ferrites show a good ferromagnetic behavior with high values of saturation magnetization, while zinc ferrite showed less magnetic behavior. High magnetization values of the samples make them suitable fillers in the conducting polymer matrix. The EMI shielding behavior of

the ferrite-PANI composites have been intensively studied over the frequency range of *X* band. The dependence of SE_A on magnetic parameters shows that better absorption value can be obtained for material with high magnetization. The addition of nano-sized ferrites to the polyaniline created more interfacial dipolar polarization and scattering which resulted to the high values of shielding effectiveness. The composites showed an excellent shielding effectiveness with almost steady values of 48–50 dB for $NiFe_2O_4$-PANI and 46–52 dB for the $CoFe_2O_4$-PANI in the entire *X* band frequency range which makes them suitable candidates as EMI shielding materials.

Acknowledgments Authors are thankful to Physics Department, Hindu College, University of Delhi and Head, Department of Physics and Astrophysics, University of Delhi. We acknowledge the University Science Instrumental Centre (USIC), Prof. Vinay Gupta, University of Delhi and National Physical Laboratory (NPL), New Delhi, for the characterization facilities and their valuable suggestions regarding the present work.

References

1. Cheng, Y.L., Dai, J.M., Zhu, X.B., Wu, D.J., Sun, Y.P.: Mater Res Bull. **45**, 663–667 (2010)
2. Micheli, D., Pastore, R., Apollo, C., Marchetti, M., Gradoni, G., Primiani, V.M.: IEEE Trans Micr Theory Tech. **59**, 2633–2646 (2011)
3. Ott, H.W.: Wiley, 2nd edn, New York (1988)
4. Wilson, P.F., Ma, M.T., Adams, J.W.: IEEE Transactions on Electromagnetic Compatibility. **30**(3), 251–259 (1988)
5. Olmedo L., Hourquebie P., Jousse F.: Wiley. Chichester Vol. 2, (1997)
6. Ting, T.H., Yu, R.P., Jau, Y.N.: Materials Chemistry and Physics. **126**, 364–368 (2011)
7. Hosseini, S.H., Asadnia, A.: Journal of Nanomaterials. **2012**, 1–6 (2012)
8. Przemyslaw, L., Lukomska, A., Jeziorska, R.: Polimery. **61**, 663–669 (2016)
9. Seong, H.K., Soon, H.J., Sung, W.B., Jun, Y.L., Jin, S.J., Sung, H.J., Myung-Ja, P.: Journal of Applied Polymer Science. **87**, 1969–1974 (2003)
10. Park, K.Y., Lee, S.E., Kim, C.G., Han, J.H.: Composite Structures. **81**, 401–406 (2007)
11. Gairola, S.P., Verma, V., Kumar, L., Dar, M.A., Annapoorni, S., Kotnala, R.K.: Synth. Met. **160**, 2315–2318 (2010)
12. Ismail, M.M., Jaber, N.A.: J. Supercond. Nov. Magn. **31**, 1917–1923 (2017)
13. Lakshmi, K., John, H., Mathew, K.T., Joseph, R., George, K.E.: Acta Mater. **57**, 371–375 (2009)
14. Tang, J., Ma, L., Tian, N., Gan, M.Y., Xu, F.F., Zeng, J.: Mater Sci Eng B. **186**, 26–32 (2014)
15. Liangchao, L., Jiang, J., Xu, F.: Mater Lett. **61**, 1091–1096 (2007)
16. Jiang, J., Ai, L.H.: Mater Lett. **62**, 3643–3645 (2008)
17. Jiang, J., Li, L., Xu, F.: Mater Sci Eng A. **456**, 300 (2007)
18. Lee, S.P., Chen, Y.J., Ho, C.M., Chang, C.P., Hong, Y.S.: Mater Sci Eng B. **143**, 1–24 (2007)
19. Jiang, J., Ai, L.H., Liu, L.Y.: Mater Lett. **64**, 888–890 (2010)
20. Elsayed, A.H., MohyEldin, M.S., Elsyed, A.M., AboElazm, A.H., Younes, E.M., Motaweh, H.A.: Int. J. Electrochem. Sci. **6**, 206–221 (2011)
21. Boeva, Z.A., Sergeyev, V.G.: Polymer Science. **56**, 144–153 (2014)
22. Suryanarayana C, Nortan MG: Plenum Publishing Corporation, (1998)
23. Ramgir, N.S., Hwang, Y.K., Mulla, I.S., Chang, J.S.: Solid State Sciences. **8**, 359–362 (2006)
24. Carbonin, S., Martignago, F., Menegazzo, G., Negro, A.: Phys. Chem. Miner. **29**, 503–514 (2002)
25. Berkowitz, A.E., Schuele, W.: J. Appl. Phys. **30**, 134–139 (1959)
26. Perez, O.P., Sasaki, H., Kasuya, A., Jeyadevan, B., Tohji, K., Hihara, T., Sumiyama, K.: J. Appl. Phys. **91**, 6958–6963 (2002)
27. Mott, N.F.: Phil. Mag. **19**, 835 (1969)
28. Hemeda, O.M., Barakat, M.M.: Journal of Magnetism and Magnetic Materials. **223**, 127–132 (2001)
29. Rafeeq, S.N., Mukhils, M.M., Sulaiman, M.A.: J. Magn. **22**(3), 406–413 (2017)
30. Joshi, S., Kumar, M., Chhoker, S., Srivastava, G., Jewariya, M., Singh, V.N.: J. Molecular Structure. **1076**, 55–62 (2014)
31. Lia, D.Y., Sun, Y.K., Gao, P.Z., Zhang, X.L., Ge, H.L.: Ceram. Int. **40**, 16529 (2014)
32. O'Neill, H., Nevnorsky, A.: American Mineralogist. **6E**, 181–194 (1983)
33. Wang, C., Shen, Y., Wang, X., Zhang, H., Xie, A.: Mater. Sci. Semiconductor Proc. **16**, 77–82 (2013)
34. Jacobo, S.E., Aphesteguy, J.C., Anton, R.L., Schegoleva, N.N., Kurlyandskaya, G.V.: European Polymer Journal. **43**, 1333–1346 (2007)
35. Konyushenko, E.N., Kazantseva, N.E., Stejskal, J., Trchová, M., Kovářová, J., Sapurina, I., Tomishko, M.M., Demicheva, O.V., Prokeš, J.: Journal of Magnetism and Magnetic Materials. **320**, 231–240 (2008)
36. Yavuz, Ö., Ram, M.K., Aldissi, M., Poddar, P., Hariharan, S.: Journal of Materials Chemistry. **15**, 810–817 (2005)
37. Li, L., Xiang, C., Liang, X., Hao, B.: Synth. Met. **160**, 28–34 (2010)
38. Khafagy, R.M.: J. Alloys Compd. **509**, 9849–9857 (2011)
39. Song, Q., Zhang, Z.J.: J. Amer. Chem. Soc. **126**, 6164–6168 (2004)
40. Singh, K., Ohlan, A., Saini, P., Dhawan, S.K.: Polym. Adv. Technol. **19**, 229 (2008)
41. Gholampoor, M., Movassagh, F., Salimkhani, H.: Solid State Sci. **64**, 51–61 (2017)
42. Mahmoodi, M., Arjmand, M., Sundararaj, U., Park, S.: Carbon. **50**, 1455–1464 (2012)
43. Ismail, M.M., Rafeeq, S.N., Sulaiman, J.M., Mandal, A.: Applied Physics A. **124**, 380 (2018)
44. Ding, Y., Liao, Q., Liu, S., Guo, H., Sun, Y., Zhang, G., Zhang, Y.: Sci. Rep. **6**, 1–9 (2016)
45. Gandhi, N., Singh, K., Ohlan, A., Singh, D.P., Dhawan, S.K.: Composites Science and Technology. **71**, 1754–1760 (2011)
46. Khairy, M.: Synthetic Metals. **189**, 34–41 (2014)
47. Bateer, B., Zhang, J., Zhang, H., Zhang, X., Wang, C., Qi, H.: J. Electron. Mater. **47**, 292–298 (2018)
48. Yan, F., Guo, D., Zhang, S., Li, C., Zhu, C., Zhang, X., Chen, Y.: Nanoscale. **10**, 2697–2703 (2018)
49. Hosseinia, S.H., Mohsenib, S.H., Asadniac, A., Kerdarid, H.: Journal of Alloys and Compounds. **509**, 4682–4687 (2011)
50. Wang, W., Gumfekar, S.P., Jiao, Q., Zhao, B.: J. Mater. Chem. C. **1**, 2851–2859 (2013)
51. Aphesteguy, J.C., Damiani, A., DiGiovanni, D., Jacobo, S.E.: Physica B. **407**, 3168–3171 (2012)
52. Ali, N.N., Atassi, Y., Salloum, A., Charba, A., Malki, A., Jafarian, M.: Materials Chemistry and Physics. **211**, 79–87 (2018)

Publisher's Note Springer Nature remains neutral with regard to jurisdictional claims in published maps and institutional affiliations.